Frequency-network mechanism for alignment of diatomic molecules by multipulse excitation

Hiroya Abe and Yukiyoshi Ohtsuki*

Department of Chemistry, Graduate School of Science, Tohoku University, Sendai 980-8578, Japan

(Received 25 January 2011; published 12 May 2011)

There are several effective nonadiabatic alignment control schemes that use multilaser pulse excitation. To explain the control mechanisms in a unified manner through a case study, we apply nonresonant optimal control simulation to a rovibrational model of N_2. For experimental feasibility, we introduce a penalty and/or constraint to the simulation to impose restrictions on the number of optically accessible rotational states. When the control time is set to one rotational period, optimal pulses with linear polarization and a wavelength of around 800 nm are composed of three subpulses. From the power spectra of the intensities of the optimal pulses, we see that the optimal pulses construct a frequency network that connects the lowest three rotational Raman transitions. The frequency-network mechanism is confirmed by calculating the degree of alignment using sets of three Gaussian pulses. It shows several combinations of pulses that (approximately) satisfy the frequency-network condition, which can explain why there exist several control schemes that achieve a high degree of alignment.

DOI: 10.1103/PhysRevA.83.053410 PACS number(s): 32.80.Qk, 37.10.Vz, 33.80.−b, 33.20.Sn

I. INTRODUCTION

The control of molecular alignment realizes a macroscopically anisotropic ensemble of molecules that have a wide range of applications, including the stereodynamics of chemical reactions [1], the elucidation of molecular structures [2–7], and so on [8–12]. Because the realization of molecular alignment in an external-field-free condition is often required, a laser pulse with a temporal width that is much shorter than a rotational period is typically employed to create a rotational wave packet [13–27]. When the wavelength of the laser pulse is around 800 nm, a rotational wave packet is created by an induced dipole interaction averaged over fast optical oscillations. Within the polarizability interaction, i.e., the lowest-order induced dipole interaction, the molecular system follows the square of a pulse envelope function [28,29]. After the laser pulse excitation, a highly aligned state appears at regular time intervals (a rotational revival), which is explained by the nonlinear dependence of the rotational energy on a quantum number [30,31].

A single-pulse excitation is known to impose restrictions on the achievement of the degree of alignment [17,18]. This was recently confirmed by the quantum-state-selected experiment of Ghafur *et al.* [26]. Multipulse excitations are, thus, required to enhance molecular alignment. For example, Leibscher *et al.* proposed optimal two- and three-pulse schemes, the timings of which are consistent with their "accumulative squeezing" scheme [17,18]; that is, the last pulses, the intensities of which are much higher than those of the previous pulses, appear at the timing of the maximal degree of alignment. Lee *et al.*, on the other hand, proposed another double-pulse scheme in which the second pulse, the intensity of which is comparable to that of the first pulse, is applied immediately before the timing of the maximal degree of alignment [21]. This enhancement mechanism can be explained by the swing analogy for rotational wave packets. In the repetitively kicked scheme of Cryan *et al.*, eight equally spaced pulses are applied to nitrogen molecules and the degree of alignment approaches the theoretical maximum value; however, the control time is about ten times longer than the former two schemes [25]. Suzuki *et al.* reported an optimal control experiment of cold nitrogen molecules with the degree of alignment as feedback and obtained a doubly peaked pulse as an optimal alignment pulse [24]. Because of the availability of various effective control schemes, it is natural to consider why the different control schemes can achieve a similarly high degree of alignment.

The purpose of the present numerical study is to answer in part the above question by means of optimal control simulation through a case study of the alignment control of nitrogen molecules [32–34]. In Sec. II, after introducing a rovibrational model of a nitrogen molecule, we outline the optimal control procedure. In Sec. III, numerical results are presented and the optimal pulses are examined in a frequency domain. In Sec. IV, we discuss the control mechanisms from the viewpoint of a network structure of the power spectrum by using a set of model Gaussian pulses.

II. THEORY

We consider a nitrogen molecule in its electronic ground state, which interacts with a linearly polarized laser pulse, $E(t)$. If we introduce the two nuclear coordinates, i.e., the internuclear distance, r, and the polar angle between the polarization vector of the laser pulse and the molecular axis, θ, the total Hamiltonian will be expressed as

$$H^t = H - \tfrac{1}{2}[\Delta\alpha(r)\cos^2\theta + \alpha_\perp(r)]\,[E(t)]^2, \qquad (1)$$

where H is a field-free molecular Hamiltonian and $\Delta\alpha(r) = \alpha_\parallel(r) - \alpha_\perp(r)$ is the nuclear-coordinate-dependent polarizability with $\alpha_\parallel(r)$ [$\alpha_\perp(r)$] being the component parallel [perpendicular] to the molecular axis. Here, we assume that the dynamical polarizability, which includes the contribution from the excited electronic states, can be approximated by a static one as we consider the laser frequencies ($\lambda \sim 800$ nm)

*Author to whom correspondence should be addressed: ohtsuki@m.tohoku.ac.jp

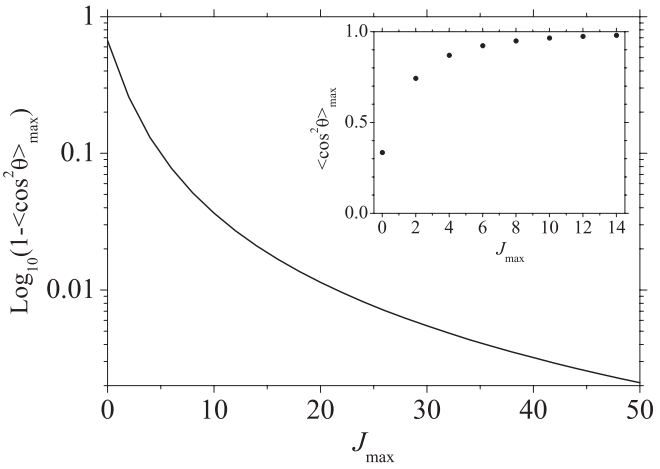

FIG. 1. Maximum expectation values of $\cos^2\theta$ calculated by assuming a rigid rotor with the given number of rotational states that is specified by $J_{\max}$. The inset provides a magnified view.

well below the electronic transition frequencies. The field-free Hamiltonian is given by

$$H = -\frac{\hbar^2}{2\mu}\frac{1}{r^2}\frac{\partial}{\partial r}\left(r^2\frac{\partial}{\partial r}\right) + \frac{J^2}{2\mu r^2} + V(r), \tag{2}$$

where μ is the reduced mass, $V(r)$ is the internuclear potential, and J is the angular momentum operator. Because of the symmetry of the system, the azimuth angle does not appear in Eq. (2) so that the quantum number associated with the projection on a space-fixed frame is conserved. In the present study, we assume that the time evolution of the molecular system is described by the time-dependent Schrödinger equation:

$$i\hbar\frac{\partial}{\partial t}|\psi(t)\rangle = H^t|\psi(t)\rangle \quad . \tag{3}$$

To design an optimal pulse, we introduce an objective functional, $F = \langle\psi(t_{\rm f})|W|\psi(t_{\rm f})\rangle$, that evaluates the degree of alignment by using a target operator, W, at a specified final time, $t_{\rm f}$. The optimal pulse is defined by a pulse that maximizes the functional, F [32–36]. Because the expectation value of $\cos^2\theta$ is often used to evaluate the degree of alignment, it would be natural to choose it as a target operator. A rotational wave packet with an extremely high degree of alignment, on the other hand, involves highly excited rotational states that are not easily optically accessible. For practical purposes, we need to impose a restriction on the rotational excitation while achieving a "reasonably" high degree of alignment. To estimate the number of rotational states required for this purpose, Fig. 1 shows the maximum expectation values of $\cos^2\theta$, assuming a rigid rotor. As shown in the inset of Fig. 1, for example, the wave packet consisting of rotational states of up to $J_{\max} = 8$ can lead to the maximum expectation value of $\langle\cos^2\theta\rangle_{\max} = 0.948$. To explicitly specify the rotational states, we introduce a projector, P, whereby the target operator is expressed as $W = P\cos^2\theta\,P$. Another way to design an experimentally feasible laser pulse is to impose a restriction on the peak intensity. This can be done, for example, by introducing a penalty factor that is proportional to the intensity of the pulse.

An optimal pulse is derived by applying the calculus of variations to the objective functional, F, under the constraint of Eq. (3). If we introduce the Lagrange multiplier, $|\xi(t)\rangle$, associated with this constraint, the first-order variational optimality condition will be represented by

$$\mathrm{Im}\langle\xi(t)|[\Delta\alpha(r)\cos^2\theta + \alpha_\perp(r)]\,|\psi(t)\rangle = 0, \tag{4}$$

where $\mathrm{Im}\langle\cdots\rangle$ denotes the imaginary part of $\langle\cdots\rangle$. The equation of motion for the Lagrange multiplier is given by

$$i\hbar\frac{\partial}{\partial t}|\xi(t)\rangle = (H^t)^\dagger|\xi(t)\rangle, \tag{5}$$

with the final condition, $|\xi(t_{\rm f})\rangle = W|\psi(t_{\rm f})\rangle$. If we assume zero temperature or a specified initial state, the optimal pulse will be obtained by solving the coupled pulse-design equations that consist of Eqs. (3), (4), and (5). The finite-temperature effects on the alignment control will be discussed in Sec. III.

The coupled pulse-design equations are solved by an iterative method. Here, we adopt the iterative procedure reported in our previous papers, in which the laser field, $E(t)$, is artificially divided into two components, $E_1(t)$ and $E_2(t)$ [33,34]. All the equations associated with the pulse design are expressed as the symmetrical sum of products of these artificially divided components. Assuming that the iteration starts by solving $|\psi^{(0)}(t)\rangle$ with an appropriate set of initial trial fields, $E_1^{(0)}(t)$ and $E_2^{(0)}(t)$, the monotonically convergent algorithm at the kth iteration step is summarized as follows:

$$i\hbar\frac{\partial}{\partial t}|\xi^{(k)}(t)\rangle = \left\{H - \frac{1}{2}[\Delta\alpha(r)\cos^2\theta + \alpha_\perp(r)]^\dagger\,E_p^{(k)}(t)\,E_q^{(k-1)}(t)\right\}|\xi^{(k)}(t)\rangle, \tag{6}$$

with the final condition, $|\xi^{(k)}(t_{\rm f})\rangle = W|\psi^{(k-1)}(t_{\rm f})\rangle$, and

$$i\hbar\frac{\partial}{\partial t}|\psi^{(k)}(t)\rangle = \left\{H - \frac{1}{2}[\Delta\alpha(r)\cos^2\theta + \alpha_\perp(r)]\,E_p^{(k)}(t)\,E_q^{(k)}(t)\right\}|\psi^{(k)}(t)\rangle, \tag{7}$$

with the initial condition $|\psi^{(k)}(t=0)\rangle = |\psi_0\rangle$. Suffixes $p$and $q$represent $(p, q) = (1, 2)$ or $(p, q) = (2, 1)$. The artificially divided components of the optimal pulse are given by

$$E_p^{(k)}(t) = E_p^{(k-1)}(t) - \lambda_p^{(k)}(t)\mathrm{Im}\langle\xi^{(k)}(t)| \times [\Delta\alpha(r)\cos^2\theta + \alpha_\perp(r)]|\psi^{(k-1)}(t)\rangle E_q^{(k-1)}(t) \tag{8}$$

$$E_q^{(k)}(t) = E_q^{(k-1)}(t) - \lambda_q^{(k)}(t)\mathrm{Im}\langle\xi^{(k)}(t)| \times [\Delta\alpha(r)\cos^2\theta + \alpha_\perp(r)]|\psi^{(k)}(t)\rangle E_p^{(k)}(t). \tag{9}$$

Here, $\lambda_1^{(k)}(t)$ and $\lambda_2^{(k)}(t)$ are step-dependent positive functions that characterize the searching speed and accuracy. The algorithm guarantees that the artificially divided components converge to the same electric field, $\lim_{k\to\infty} E_1^{(k)}(t) = \lim_{k\to\infty} E_2^{(k)}(t) = E(t)$, as all the equations in the algorithm have a symmetric form with respect to $E_1(t)$ and $E_2(t)$.

In practice, it is useful to minimize the difference between $E_1^{(k)}(t)$ and $E_2^{(k)}(t)$ during the iteration to improve the convergence behavior. For this purpose, we can alternately set $(p, q) = (1, 2)$ and $(p, q) = (2,1)$ as the iteration. By doing so, symmetry with respect to suffixes, $E_p^{(k)}(t)$ and $E_q^{(k)}(t)$, is introduced into the algorithm. A more direct way to minimize the difference would be to replace $E_1^{(k)}(t)$and $E_2^{(k)}(t)$ with, for example, $[E_1^{(k)}(t) + E_2^{(k)}(t)]/2$, at each iteration step. As this replacement can sustain the high numerical accuracy, which is discussed in the Appendix and also confirmed numerically in Sec. III, we employ this latter method in the present study.

Finally, we summarize the numerical details. We assume a Morse potential for the intramolecular potential, $V(r)$, the parameters of which are taken from Ref. [37]. The equilibrium distance, $r_e = 1.10$ Å, leads to the rotational constant, $B = 2.00\ \mathrm{cm}^{-1}$, which corresponds to the rotational period, $T_{\mathrm{rot}} = 8.35$ ps. Although our simulations explicitly include the vibrational degree of freedom, in the following numerical results, the time and energy (frequency) are measured in units of T_{rot} and B, respectively, for convenience. The nuclear-coordinate-dependent polarizability components are taken from Ref. [38]. In numerically integrating the Schrödinger equation, we expand the wave function in terms of the zero-order states $\{|\mathrm{v}\ J\rangle\}$, in which $|\mathrm{v}\rangle$ and $|J\rangle$ are the eigenstates of

$$H_{\mathrm{vib}}^{(0)} = -\frac{\hbar^2}{2\mu}\frac{1}{r^2}\frac{\partial}{\partial r}\left(r^2\frac{\partial}{\partial r}\right) + V(r) \quad \text{and} \quad H_{\mathrm{rot}}^{(0)} = \frac{J^2}{2\mu r_e^2} \tag{10}$$

respectively. The maximum quantum numbers are set to $\mathrm{v} = 2$ and $J = 14$. (We have checked the convergence with respect to the number of basis functions by comparing the results with those obtained by adopting a larger basis.) In the present study, the final time is set to $t_{\mathrm{f}} = T_{\mathrm{rot}}$ and the time evolution of the expansion coefficients is calculated by the fifth-order Runge-Kutta method with the number of time grids being 10^6 (in Figs. 2 and 3) and 5×10^5 (in other figures). In the iterative calculations, the convergence parameters are set to a step-independent constant, $\lambda_1^{(k)}(t) = \lambda_2^{(k)}(t) = 10^{38}$ (in SI units).

III. NUMERICAL RESULTS

In the first example, the target operator is chosen as $W = P\cos^2\theta\ P$, in which the projector, P, is expressed, in terms of the zero-order rotational states [Eq. (10)], as

$$P = \sum_{j=0}^{J_{\max}/2} |2j\rangle\langle 2j|, \quad \text{with} \quad J_{\max} = 8. \tag{11}$$

From Fig. 1, the theoretical maximum value of the degree of alignment is 0.948. In Fig. 2(a), the convergence behavior is shown as a function of the number of iteration steps when the calculation starts with an initial guess field:

$$E_1^{(0)}(t) = E_2^{(0)}(t) = \begin{cases} \varepsilon_0 \sin(\pi t/2\tau)\sin(\omega t) & (0 \leqslant t \leqslant \tau) \\ \varepsilon_0 \sin(\omega t) & (\tau \leqslant t \leqslant t_{\mathrm{f}} - \tau) \\ \varepsilon_0 \sin[\pi (t_{\mathrm{f}} - t)/2\tau]\sin(\omega t) & (t_{\mathrm{f}} - \tau \leqslant t \leqslant t_{\mathrm{f}}) \end{cases} \tag{12}$$

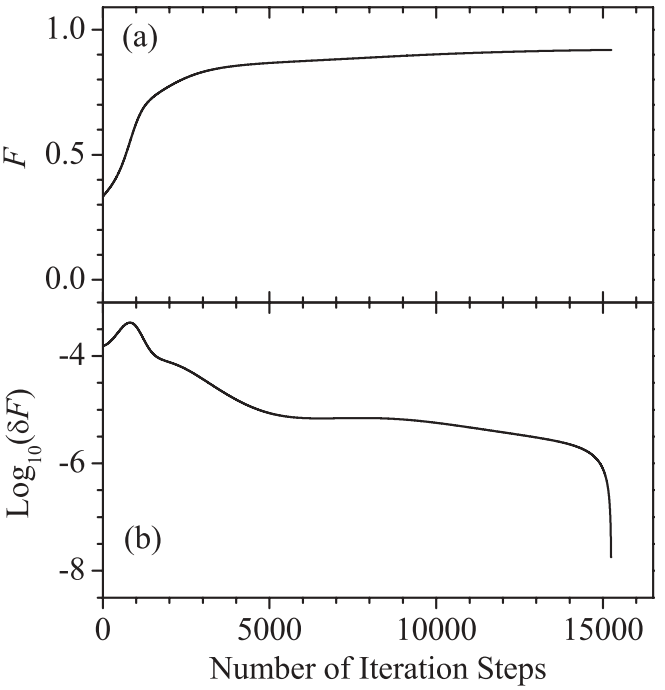

FIG. 2. Convergence behavior of the present monotonically convergent algorithm is shown by (a) the values of objective functional as a function of iteration steps, and (b) the values of the difference in objective functional between adjacent iteration steps.

with $\varepsilon_0 = 0.8$ GV/m and $\tau = 3$ ps. The carrier frequency, ω, corresponds to $\lambda = 800$ nm. The convergence is defined by the value of the objective functional at the final iteration step, beyond which further monotonic convergence breaks down due to numerical limitations. Figure 2(b) shows the values of the difference in objective functional between the adjacent iteration steps, which give an indication of the search precision. Even with the modification (see Appendix), the present algorithm can search the optimal solution with an accuracy of up to $\delta F \sim 10^{-8}$, which can validate the present modification.

Figure 3 shows (a) the optimal pulse as a function of time, and (b) the time evolution of the degree of alignment and (c) that of the populations associated with the zero-order rotational states [Eq. (10)]. The optimal pulse consists of three subpulses and leads to $\langle\psi(t_f)|\cos^2\theta\,|\psi(t_f)\rangle = 0.933$, which is close to the ideal value of 0.948. Roughly speaking, the first subpulse creates the $J = 0$ and 2 superposition state, the most intense second subpulse excites a number of rotational states (wave packet), and the third subpulse adjusts the shape of the rotational states. The latter two subpulses appear at the timings when the rotational wave packet has a large kinetic energy; this could be qualitatively understood in terms of the swing analogy [21]. As regards the vibrational excitation, it contributes little to the improvement of the alignment control, as shown in Fig. 4. This is mainly because centrifugal distortion, i.e., rovibrational coupling, can be neglected in the present system.

To further suppress the peak intensity while sustaining a high degree of alignment, we next design the optimal pulse by introducing a penalty term. The penalty is given by a positive constant, γ, and is included in the polarizability interaction such that $(1 + i\,\gamma)\Delta\alpha$. It represents the penalty

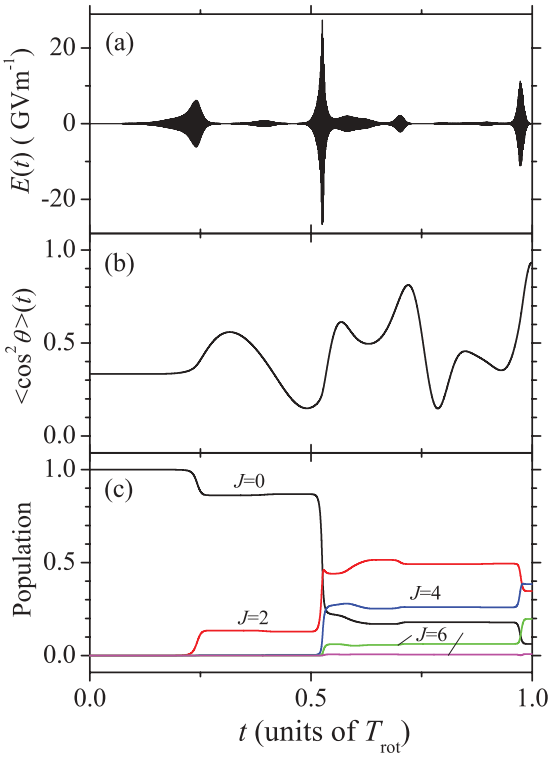

FIG. 3. (Color online) (a) Optimal pulse, (b) degree of alignment, $\langle\cos^2\theta\rangle(t) \equiv \langle\psi(t)|\cos^2\theta|\psi(t)\rangle$, and (c) populations of zero-order rotational states [Eq. (10)] as a function of time. Time is measured in units of rotational period, $T_{\rm rot} = 8.35$ ps (see text).

due to instantaneous pulse intensity; that is, a higher pulse intensity leads to a smaller norm of the wave function, and this results in the decrease in the degree of alignment. The optimal pulse in Fig. 5(a) is calculated by employing the target operator $W = \cos^2\theta$, $\gamma = 0.01$, and the initial trial field in Eq. (12). The overall convergence behavior is quite similar to that in Fig. 2 except that the present calculation needs about 15000 iteration steps (not shown). This optimal pulse is substituted into the original equation of motion to calculate (b) the time evolution of the degree of alignment and (c) that of the populations of the zero-order rotational states. The optimal pulse in Fig. 5(a) consists of three subpulses with similar peak amplitudes. Although the optimal pulse has almost a half of the peak amplitude (a quarter of the peak intensity) of that in Fig. 3, it leads to a similar degree of alignment, 0.918, to that in Fig. 3(b). By comparing the time evolution of the populations in Fig. 5(c) with that in Fig. 3(c), we find that the optimal pulses in both figures seem to share common control mechanisms.

Note that in our trials, we almost always obtain a set of three subpulses as the optimal solution, independent of the initial trial fields, the magnitude of the penalty factors, etc. As for the optimal pulses in Figs. 3(a) and 5(a), the second subpulses are accompanied by small substructures; however, they make a tiny contribution to the improvement of the degree of alignment. For example, if we remove such substructures from the optimal pulse in Fig. 5(a), the degree of alignment is reduced by only 0.009. This numerical result suggests that the three-pulse control is essential for the present target, as long as we set the control time to around $t_{\rm f} = T_{\rm rot}$.

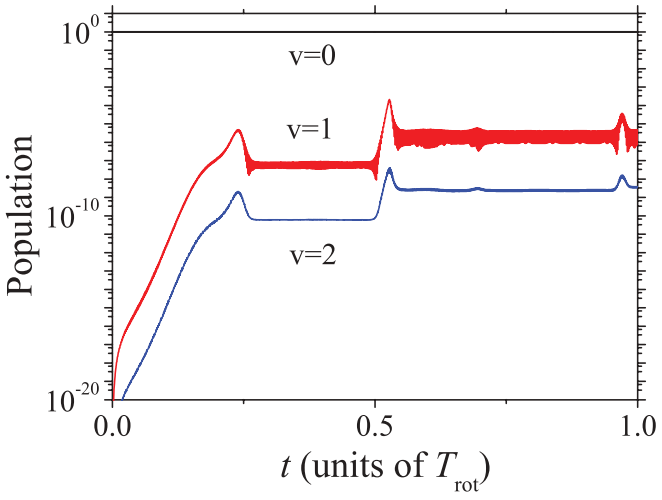

FIG. 4. (Color online) Populations of zero-order vibrational states [Eq. (10)] as a function of time, which are plotted in the logarithmic scale. Time is measured in units of rotational period, $T_{\rm rot}$.

To examine the finite-temperature effects on the control achievement, in Fig. 6, we show the time evolution of the degree of alignment under the irradiation of the optimal pulse in Fig. 5(a) for the six different temperatures. We assume that the ensemble of nitrogen molecules consists of pure $^{14}_{7}N_2$ isotopes. Because we have already seen from Fig. 4 that rovibrational coupling is safely neglected, the zero-order rotational states are physically meaningful states. We thus attribute the statistical weights to the zero-order rotational states to construct the initial thermal distribution, in which we take into account the restrictions on the symmetry of rotational

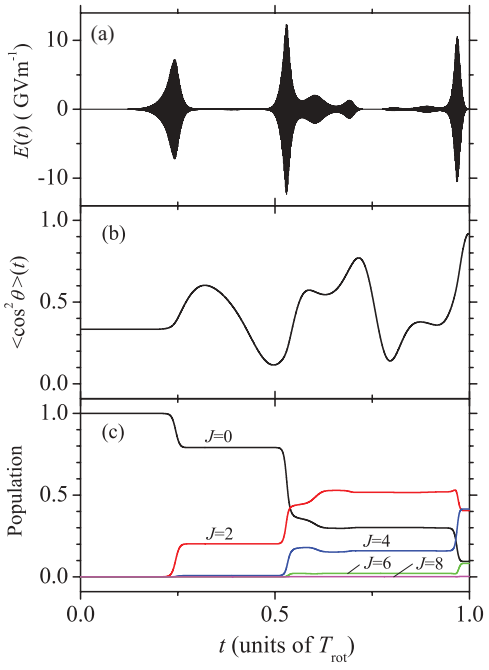

FIG. 5. (Color online) (a) Optimal pulse, (b) degree of alignment, $\langle\cos^2\theta\rangle(t)$, and (c) populations of zero-order rotational states [Eq. (10)] as a function of time. Time is measured in units of rotational period, $T_{\rm rot}$.

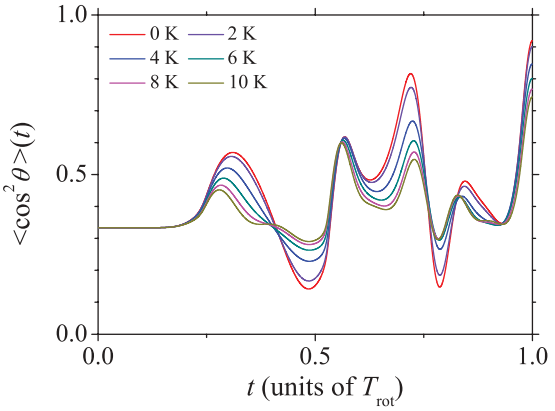

FIG. 6. (Color online) Finite-temperature effects on the degree of alignment. The degrees of alignment have values of 0.918 ($T = 0$ K), 0.895 ($T = 2$ K), 0.831 ($T = 4$ K), 0.782 ($T = 6$ K), 0.748 ($T = 8$ K), and 0.723 ($T = 10$ K) at $t_f = T_{rot}$.

states imposed by the nuclear spin, $I = 1$. Even in the worst case of $T = 10$ K, the degree of alignment still shows a high value of 0.723 even though only one-third of the population (0.351) is initially distributed in the $J = 0$ state. In Fig. 6, a higher temperature leads to the less prominent oscillating behavior of the time evolution of $\langle\cos^2\theta\rangle$. Its fundamental revival structure, however, is kept within the temperatures considered here, which makes the three-pulse control scheme effective even in the finite-temperature case. This can be in part attributed to the fact that the rotational states with even quantum numbers have larger statistical weights than those with odd numbers because of the nuclear spin multiplicity.

Figure 7 shows the structure of the optimal pulse in Fig. 5(a) in a frequency domain. As the molecule interacts with the square of the electric field, $[E(t)]^2$, we calculate its power spectrum defined by

$$I(\omega) = \left| \int_{-\infty}^{\infty} dt\, e^{-i\omega t}\, \overline{[E(t)]^2} \right|^2, \tag{13}$$

where the bar above $[E(t)]^2$ means the cycle average over the carrier frequency. Figure 7(a) shows the power spectrum together with that of each subpulse. Each subpulse has a simple Gaussian-like structure and is gradually broadened in temporal order, reflecting the increase in the number of rotational states involved in the wave packet. The overall structure, on the other hand, consists of well-separated frequency components that can be regarded as an interferogram due to the difference in the temporal peak of the subpulses. We can see three kinds of frequency progressions. Those frequency progressions can be assigned by assuming a rigid rotor model because we can safely neglect the contribution of the vibrational degree of freedom (Fig. 4). If we measure the frequency in units of $2B$ with B being the rotational constant, those progressions can be referred to as $a_n = 7n$, $b_n = 7n + 3$, and $c_n = 7n + 4$ for $n = 0, 1, 2, \ldots$ ($a_{-n} = -a_n$, $b_{-n} = -c_{n-1}$, and $c_{-n} = -b_{n-1}$ for $n = 1, 2, \ldots$). The three progressions construct a frequency network. As will be discussed in Sec. IV in detail, the frequency network is the key to achieving a high degree of alignment and understanding the control mechanisms.

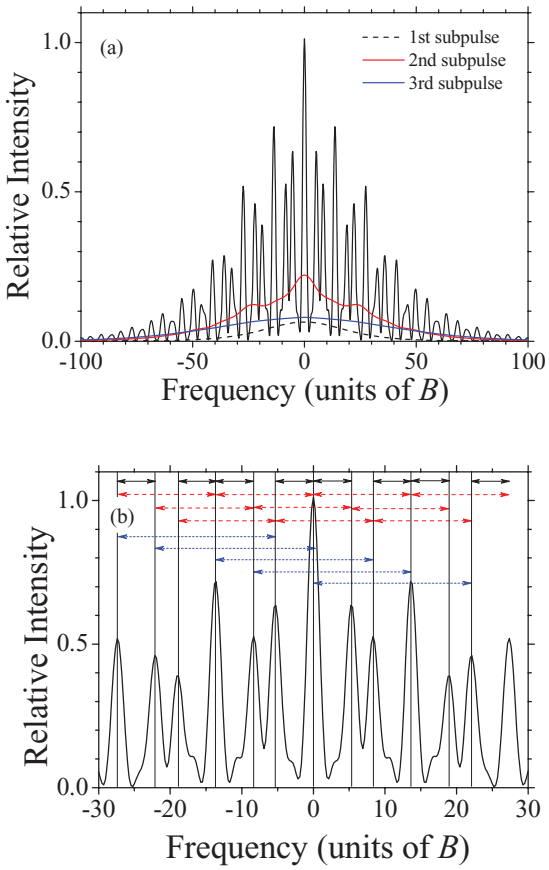

FIG. 7. (Color online) Power spectrum of the intensity of the optimal pulse in Fig. 5(a) [see Eq. (13)], in which the spectra of the first, second, and third subpulses are shown by black-dashed (lower), red (upper), and blue (middle) lines, respectively. (b) Magnified view of (a) together with a portion of assignments associated with Raman transitions. Solid, dashed, and dotted arrows represent $|J = 2\rangle \leftarrow |J = 0\rangle$, $|J = 4\rangle \leftarrow |J = 2\rangle$, and $|J = 6\rangle \leftarrow |J = 4\rangle$ transition frequencies, respectively.

The present frequency network connects the lowest three rotational states through the Raman transitions. To explain this, we consider the origin of the numbers that characterize the progressions. Note that the frequencies associated with the lowest three rotational Raman transitions are 3 ($|J = 2\rangle \leftarrow |J = 0\rangle$), 7 ($|J = 4\rangle \leftarrow |J = 2\rangle$), and 11 ($|J = 6\rangle \leftarrow |J = 4\rangle$) in units of $2B$. As shown in Fig. 7(b), the differences between the adjacent components in each progression correspond to the $|J = 4\rangle \leftarrow |J = 2\rangle$ transitions. The combination of a_n and b_n and that of a_n and c_n also correspond to the frequencies of the Raman transitions, while that of b_n and c_n does not. This explains why the intensities of the a_n components are higher than those of b_n and c_n.

IV. DISCUSSION

The power spectrum of the intensity of the optimal pulse suggests that the frequency network that connects the rotational states through the Raman transitions is essential to achieve a high degree of alignment. To examine the alignment control mechanisms in a unified manner, we generalize this idea by adopting a set of three Gaussian subpulses, the total

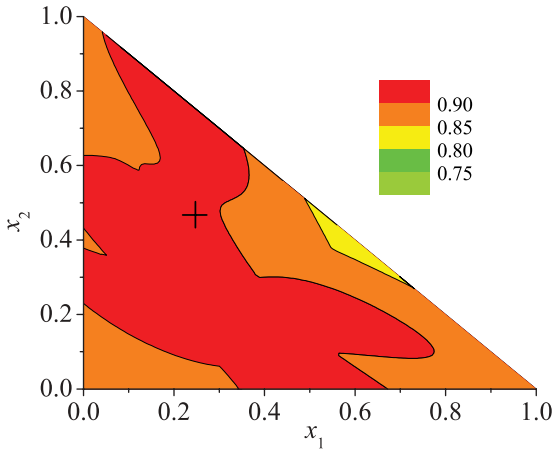

FIG. 8. (Color online) Effects of relative intensities of Gaussian subpulses on the degree of alignment [see Eq. (14)]. The plus (+) in the figure indicates the position of relative intensities corresponding to the optimal pulse in Fig. 5(a).

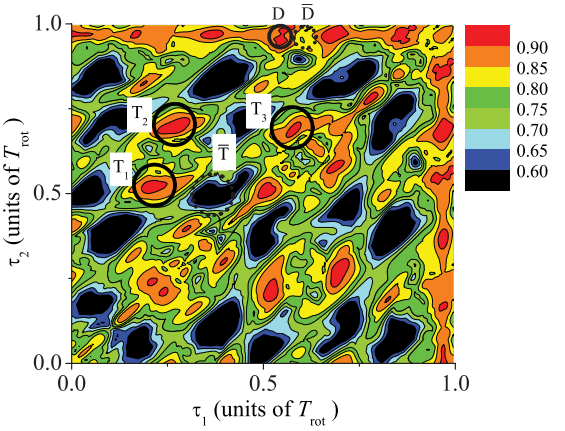

FIG. 9. (Color online) Effects of the timing of the 1st and 2nd Gaussian subpulses on the degree of alignment [see Eq. (14)]. Regions specified by T_1, T_2, and T_3 ($\bar{T}$) represent those associated with the high (low) degree of alignment in the case of triple-pulse excitation. The region specified by D ($\bar{D}$) represents that with the high (not-so-high) degree of alignment in the case of double-pulse excitation.

fluence of which is set to a value that is the same as that of the optimal pulse in Fig. 5(a). The control pulse is expressed as the sum of Gaussian subpulses:

$$E(t) = \sum_{j=1}^{3} \sqrt{x_j}\, \varepsilon_G \exp\left[-\frac{(t-\tau_j)^2}{2\sigma^2}\right] \cos(\omega t), \qquad (14)$$

where x_j is the parameter that determines the relative intensity of the jth subpulse and the normalization condition is defined by $x_1 + x_2 + x_3 = 1$. The temporal peak position of the jth subpulse is specified by τ_j. The wavelength of the carrier frequency is set to 800 nm. The amplitude and the pulse temporal width parameters are chosen as $\varepsilon_G = 10.0$ GV/m and $\sigma = 0.664$ ps, respectively. The value of σ is determined by the temporal width of the third subpulse in Fig. 5(a).

To see the effects of the relative intensities of the Gaussian subpulses, we calculate the degree of alignment as a function of x_1 and x_2 [see Eq. (14) and the normalization condition, $x_1 + x_2 + x_3 = 1$]. The timings of the three subpulses are set to values that are the same as those of the optimal pulse and are fixed in this calculation. Under these conditions, Fig. 8 shows the distribution of the maximum values of the degree of alignment that are found during $t \in [T_{\rm rot}, 2T_{\rm rot}]$ because of the revival structure of the rotational wave packet [31]. The degree of alignment is greater than 0.90 over a wide range of distribution, suggesting that the relative intensities of the subpulses do not play a critical role in the alignment control. In the following analyses, we thus assume a set of Gaussian subpulses with equal intensities, i.e., $x_1 = x_2 = x_3$.

Figure 9 shows the effects of the timing of the Gaussian subpulses on the control achievement, in which we calculate the degree of alignment as a function of times τ_1 and τ_2. Here, we assume a fixed time for τ_3, which is set to the same timing as that of the third subpulse of the optimal pulse in Fig. 5(a). For a given set of delay times, we can search the maximum degree of alignment after the irradiation of the pulse during $t \in [T_{\rm rot}, 2T_{\rm rot}]$. The maximum values are plotted as a function of τ_1 and τ_2 in Fig. 9. Because of our definition of the irradiation timing, the figure has a symmetric structure with respect to τ_1 and τ_2. Contrary to the results in Fig. 8, the overall structure is quite sensitive to a set of delay times. There appears a high degree of alignment in several regions that are classified into the triple-, double-, and single-pulse excitation regions.

There are three triple-pulse excitation regions specified by T_1, T_2, and T_3, one of which corresponds to the optimal solution in Fig. 5(a). As suggested in Sec. III, the frequency network is essential to achieving a high degree of alignment. In fact, these three sets of triple pulses share the same network structure. To show this explicitly, we estimate the temporal peaks of subpulses from a frequency-networked power spectrum that is assumed to be given by

$$\tilde{I}(\omega) = \tilde{I}_0 \exp\left(-\frac{\gamma^2\omega^2}{4}\right)\left\{\sum_{n=-N}^{N} \exp\left[-\frac{\sigma^2(\omega-a_n)^2}{4}\right] + \sum_{n=-N}^{N-1} \exp\left[-\frac{\sigma^2(\omega-b_n)^2}{4}\right] + \sum_{n=-N}^{N-1} \exp\left[-\frac{\sigma^2(\omega-c_n)^2}{4}\right]\right\}, \qquad (15)$$

where γ determines the envelope of the power spectrum so that $\gamma << \sigma$. The inverse Fourier transform of Eq. (15) yields

$$I(t) = I_0 \exp\left(-\frac{\eta t^2}{\sigma^2}\right)\left\{\sum_{n=0}^{N} \exp\left(-\frac{\eta\gamma^2 a_n^2}{4}\right)\cos(a_n t) + \sum_{n=0}^{N-1} \exp\left(-\frac{\eta\gamma^2 b_n^2}{4}\right)\cos(b_n t) + \sum_{n=0}^{N-1} \exp\left(-\frac{\eta\gamma^2 c_n^2}{4}\right)\cos(c_n t)\right\}, \qquad (16)$$

where $\eta = \sigma^2/(\gamma^2+\sigma^2) \simeq 1$. Figure 10 shows the envelope function when $N = 5$, in which the negative values come from the oversimplified estimation. The three prominent temporal

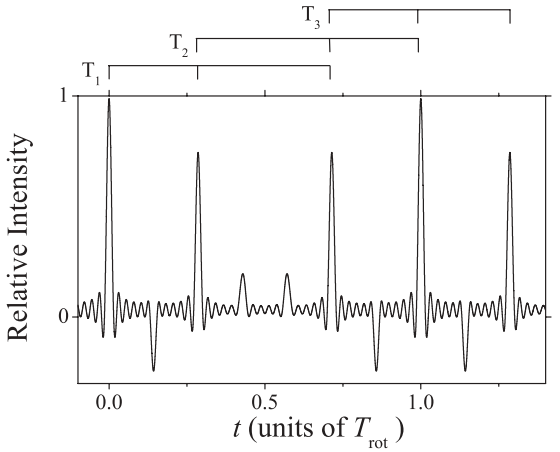

FIG. 10. Pulse envelope function reproduced from the frequency network [see Eqs. (15) and (16)].

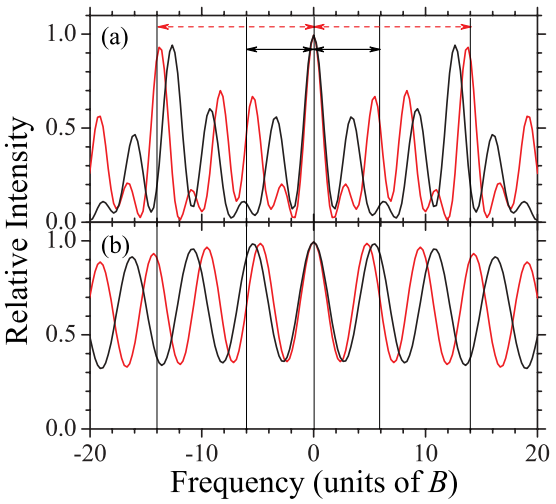

FIG. 11. (Color online) Typical examples of power spectra associated with the high [red (gray) lines] and low (black lines) degrees of alignment in the cases of (a) three-pulse and (b) double-pulse excitations. The results in (a) are taken from the regions specified by T_1 (solid circle) and $\bar{T}$ (dotted circle) in Fig. 9, and those in (b) are taken from regions D (solid circle) and $\bar{D}$ (dotted circle) in Fig. 9.

peaks within one rotational period correspond to the three sets of triple pulses that achieve a high degree of alignment. In Fig. 9, we can also see the regions associated with a low degree of alignment, in which the spectra partly lack the frequency components that are needed to construct the network.

The double-pulse excitation regions are distributed along the lines $\tau_1 = \tau_3$ and $\tau_2 = \tau_3$, in which stronger subpulses appear later than weaker subpulses. Another double-pulse excitation region lies along the line $\tau_1 = \tau_2$, in which stronger subpulses appear earlier than weaker subpulses. Some regions show a higher degree of alignment than the others depending on the timing of the excitations. Although the double-pulse excitation cannot construct the present frequency network rigorously, the power spectra associated with a high degree of alignment can approximately satisfy the frequency-network condition because of their broad bandwidths.

To examine the control mechanisms from the viewpoint of the network in more detail, Fig. 11 provides typical examples of the power spectra associated with the high [red (gray) lines] and low (black lines) degrees of alignment in the cases of (a) triple-pulse and (b) double-pulse excitations. The results in Fig. 11(a) are taken from the regions specified by T_1 and $\bar{T}$ in Fig. 9, respectively. The black line clearly lacks the frequency components associated with the $|J = 4\rangle \leftarrow |J = 2\rangle$ transition. On the other hand, the results in Fig. 11(b) are typical examples associated with the high and not-so-high degrees of alignment, which are located in regions D and $\bar{D}$ in Fig. 9, respectively. Because of the double-pulse excitation, these power spectra are composed of equally spaced frequency components. In Fig. 11(b), we see that due to the finite frequency width of each component, the intervals of the frequency components of the red line satisfy the lowest three Raman transitions, $|J = 2\rangle \leftarrow |J = 0\rangle$, $|J = 4\rangle \leftarrow |J = 2\rangle$, and $|J = 6\rangle \leftarrow |J = 4\rangle$, simultaneously. Contrary to this, the black line in Fig. 11(b) has no combination of the frequency components that satisfies the $|J = 4\rangle \leftarrow |J = 2\rangle$ transition, resulting in the decrease in the degree of alignment. The broader the width of each frequency component, the greater the chance for a pulse pair to approximately satisfy the Raman transition condition. This can explain why we see wide regions associated with a high degree of alignment, e.g., along line $\tau_1 = \tau_3$ with $\tau_2 > 0.5$ compared to that with $\tau_2 < 0.5$.

In Fig. 9, the single-pulse excitation corresponds to $\tau_1 = \tau_2 = \tau_3$. We see that a single pulse that provides a structureless network can lead to a reasonably high degree of alignment, although its achievement is known to be limited by saturation effects [17,18].

We have shown that the alignment control can be interpreted on the basis of the frequency-network mechanisms. It would be thus natural to consider the possibility of extending the size of the present network. In fact, when we set the control time to $t_f = 2\,T_{rot}$, we have an optimal pulse that contains new progressions, say, $d_n = 7n + 1$ and $e_n = 7n + 6$ for $n = 0, 1, 2, \ldots$ ($d_{-n} = -e_{n-1}$ and $e_{-n} = -d_{n-1}$ for $n = 1, 2, \ldots$) in addition to a_n, b_n, and c_n (not shown). Then, the frequency components of the original set of progressions, $\{a_n, b_n, c_n\}$, can be connected to each other through the lowest three Raman transitions, whereas those of the new progressions are partly connected to each other. Furthermore, the combination of a_n and $d_n(e_n)$ corresponds to the frequency of the higher Raman transitions $|J = 6\rangle \leftarrow |J = 4\rangle$. For a given pulse energy, the increase in the number of frequency components results in the decrease in the peak intensity of each frequency component. To increase the peak intensity subject to minimal pulse energy, the bandwidth of each frequency component needs to become narrow, which requires a long control period.

The complete frequency network leads to the repetitively kicked scheme proposed by Cryan *et al.* [25], in which an equally spaced pulse appears at every rotational period. In this sense, one may consider the similarity between the present frequency-network control scheme and the optical frequency combination approaches, although the physical objectives of the former (latter) approaches are usually the control of rotational wave packets (population transfer). As for the optical

frequency combination approaches, we would suggest the relevant studies in Refs. [39–41].

V. CONCLUSIONS

We have applied nonresonant optimal control simulation to a rovibrational model of N_2 to design a linearly polarized laser pulse with a wavelength of around 800 nm that achieves a high degree of alignment within one rotational period. We have imposed restrictions on the number of optically accessible rotational states explicitly (Fig. 3) and by adding a penalty subject to the instantaneous intensity of a laser pulse (Fig. 5). In our simulations, we saw virtually no contribution from the vibrational degree of freedom to the control achievement (Fig. 4). The designed optimal pulse consists of three subpulses, the timing of which is qualitatively examined by the swing mechanism proposed by Lee *et al.* [21] From the quantitative analyses, we found that the power spectrum of the intensity of the optimal pulse constructs the frequency network (Fig. 7). This network consists of the progressions of $a_n = 7n$, $b_n = 7n + 3$, and $c_n = 7n + 4$ in units of $2B$, and connects the lowest three rotational Raman transitions to each other. The essential role of the frequency network is confirmed by calculating the degree of alignment by using a set of three Gaussian pulses (Figs. 8 and 9). For example, the frequency network given by the optimal pulse predicts the other two sets of three subpulses that lead to a high degree of alignment, which consistently explains the calculated results. As for the double-pulse excitation, the power spectra associated with a high degree of alignment can approximately satisfy the frequency-network condition because of their broad bandwidths. There are several combinations of subpulses that (approximately) construct frequency networks, and this can explain why there exist several kinds of effective alignment control pulses. From the viewpoint of the frequency-network mechanism, the ultimate network consists of frequency components having an equal interval of $2B$, which leads to the repetitively kicked scheme predicted by Cryan *et al.* [25] One drawback of this control would be that a much longer time is taken than one rotational period. In practice, we will need to choose a suitable (approximate) network in relation to the available laser resources and the required degree of alignment.

ACKNOWLEDGMENTS

We acknowledge stimulating discussions with Professor H. Kono and Professor T. Nakajima. This work was partly supported by a Grant-in-Aid for Scientific Research (B) (20350001).

APPENDIX: CONVERGENCE BEHAVIOR OF THE MODIFIED ALGORITHM

In the present simulation, we replace $E_1^{(k-1)}(t)$ and $E_2^{(k-1)}(t)$ with the suffix-independent field, $E^{(k-1)}(t)$, after finishing the (k-1)th iteration step [33,34]. To see the convergence behavior of the modified algorithm, we calculate the difference in objective functional between the kth and (k-1)th adjacent steps, $\delta F^{(k,\,k-1)} = F^{(k)} - F^{(k-1)}$, assuming that $E_1^{(k-1)}(t)$ and $E_2^{(k-1)}(t)$ are replaced with the suffix-independent field, $E^{(k-1)}(t)$,

$$\delta F^{(k,\,k-1)} = \langle \delta\psi^{(k,\,k-1)}(t_f)|W|\delta\psi^{(k,\,k-1)}(t_f)\rangle + 2\mathrm{Re}\langle\psi^{(k-1)}(t_f)|W|\delta\psi^{(k,\,k-1)}(t_f)\rangle, \tag{A1}$$

where $|\delta\psi^{(k,\,k-1)}(t)\rangle = |\psi^{(k)}(t)\rangle - |\psi^{(k-1)}(t)\rangle$.. To express the second term of the right-hand side of Eq. (A1) in terms of an electric field, we introduce an auxiliary function,

$$P(t) = 2\mathrm{Re}\langle\xi^{(k)}(t)\,|\delta\psi^{(k,\,k-1)}(t)\rangle, \tag{A2}$$

which gives $P(t_f) = 2\mathrm{Re}\langle\psi^{(k-1)}(t_f)|W|\delta\psi^{(k,\,k-1)}(t_f)\rangle$ and $P(0) = 0$. If we differentiate Eq. (A2) with respect to time and then substitute the pulse design equations into the resultant equation, we have

$$\hbar\frac{d}{dt}P(t) = \frac{1}{\lambda_2^{(k)}(t)}\left[E_2^{(k)}(t) - E^{(k-1)}(t)\right]^2 + \frac{1}{\lambda_1^{(k)}(t)}E_1^{(k)}(t)\left[E_1^{(k)}(t) - E^{(k-1)}(t)\right] + Q(t), \tag{A3}$$

where

$$Q(t) = \mathrm{Im}\,\langle\xi^{(k)}(t)|\,\Delta\alpha\cos^2\theta|\psi^{(k-1)}(t)\rangle\,E_1^{(k-1)}(t)E_2^{(k-1)}(t). \tag{A4}$$

If we assume

$$E^{(k-1)}(t) = \frac{1}{2}\left[E_1^{(k-1)}(t) + E_2^{(k-1)}(t)\right], \tag{A5}$$

then the function $Q(t)$ can be rewritten as

$$Q(t) = -\frac{1}{\lambda_1^{(k)}(t)}E^{(k-1)}(t)\left[E_1^{(k)}(t) - E^{(k-1)}(t)\right] + O\left(\delta E^{(k-1)}(t)\right)^2, \tag{A6}$$

where

$$\delta E^{(k-1)}(t) = \frac{1}{2}\left[E_2^{(k-1)}(t) - E_1^{(k-1)}(t)\right]. \tag{A7}$$

It should be noted that in Eq. (A6), there is no term that is proportional to $\delta E^{(k-1)}(t)$. Substituting Eq. (A6) into Eq. (A3) and then integrating the resulting equation over $[0,\, t_f]$, we have

$$P(t_f) = \int_0^{t_f} dt\left\{\frac{\left[E_2^{(k)}(t) - E^{(k-1)}(t)\right]^2}{\hbar\lambda_2^{(k)}(t)} + \frac{\left[E_1^{(k)}(t) - E^{(k-1)}(t)\right]^2}{\hbar\lambda_1^{(k)}(t)} + O\left(\delta E^{(k-1)}(t)\right)^2\right\}. \tag{A8}$$

Because of $P(t_f) = 2\mathrm{Re}\,\langle\psi^{(k-1)}(t_f)|\,W\,|\delta\psi^{(k,\,k-1)}(t_f)\rangle$, the monotonic convergence is guaranteed up to the first order in $\delta E^{(k-1)}(t)$ and, therefore, the modified algorithm can work with high numerical accuracy.

[1] D. Herschbach, Eur. Phys. J. D **38**, 3 (2006).
[2] P. W. Dooley, I. V. Litvinyuk, K. F. Lee, D. M. Rayner, M. Spanner, D. M. Villeneuve, and P. B. Corkum, Phys. Rev. A **68**, 023406 (2003).
[3] J. Itatani, J. Levesque, D. Zeidler, H. Niikura, H. Pepin, J. C. Kieffer, P. B. Corkum, and D. P. Villeneuve, Nature (London) **432**, 867 (2004).
[4] J. C. H. Spence and R. B. Doak, Phys. Rev. Lett. **92**, 198102 (2004).
[5] C. Z. Bisgaard, O. J. Clarkin, G. Wu, A. M. D. Lee, O. Geßner, C. C. Hayden, and A. Stolow, Science **323**, 1464 (2009).
[6] H. Akagi, T. Otobe, A. Staudte, A. Shiner, F. Turner, R. Dörner, D. M. Villeneuve, and P. B. Corkum, Science **325**, 1364 (2009).
[7] P. Reckenthaeler, M. Centurion, W. Fuß, S. A. Trushin, F. Krausz, and E. E. Fill, Phys. Rev. Lett. **102**, 213001 (2009).
[8] R. A. Bartels, T. C. Weinacht, N. Wagner, M. Baertschy, C. H. Greene, M. M. Murnane, and H. C. Kapteyn, Phys. Rev. Lett. **88**, 013903 (2001).
[9] I. V. Litvinyuk, K. F. Lee, P. W. Dooley, D. M. Rayner, D. M. Villeneuve, and P. B. Corkum, Phys. Rev. Lett. **90**, 233003 (2003).
[10] S. Fleischer, I. Sh. Averbukh, and Y. Prior, Phys. Rev. A **74**, 041403(R) (2006).
[11] D. Pinkham, T. Vogt, and R. R. Jones, J. Chem. Phys. **129**, 064307 (2008).
[12] N. Takemoto and K. Yamanouchi, Chem. Phys. Lett. **451**, 1 (2008).
[13] D. Normand, L. A. Lompré, and C. Cornaggia, J. Phys. B **25**, L497 (1992).
[14] T. Seideman, J. Chem. Phys. **103**, 7887 (1995).
[15] F. Rosca-Pruna and M. J. J. Vrakking, Phys. Rev. Lett. **87**, 153902 (2001).
[16] F. Rosca-Pruna and M. J. J. Vrakking, J. Chem. Phys. **116**, 6579 (2002).
[17] M. Leibscher, I. Sh. Averbukh, and H. Rabitz, Phys. Rev. Lett. **90**, 213001 (2003).
[18] M. Leibscher, I. Sh. Averbukh, and H. Rabitz, Phys. Rev. A **69**, 013402 (2004).
[19] M. Renard, E. Hertz, S. Guérin, H. R. Jauslin, B. Lavorel, and O. Faucher, Phys. Rev. A **72**, 025401 (2005).
[20] C. Horn, M. Wollenhaupt, M. Krug, T. Baumert, R. de Nalda, and L. Bañares, Phys. Rev. A **73**, 031401(R) (2006).
[21] K. F. Lee, E. A. Shapiro, D. M. Villeneuve, and P. B. Corkum, Phys. Rev. A **73**, 033403 (2006).
[22] H. Hasegawa and Y. Ohshima, Phys. Rev. A **74**, 061401(R) (2006).
[23] D. Pinkham, K. E. Mooney, and R. R. Jones, Phys. Rev. A **75**, 013422 (2007).
[24] T. Suzuki, Y. Sugawara, S. Minemoto, and H. Sakai, Phys. Rev. Lett. **100**, 033603 (2008).
[25] J. P. Cryan, P. H. Bucksbaum, and R. N. Coffee, Phys. Rev. A **80**, 063412 (2009).
[26] O. Ghafur, A. Rouzée, A. Gijsbertsen, W. K. Siu, S. Stotle, and M. J. J. Vrakking, Nat. Phys. **5**, 289 (2009).
[27] L. Holmegaard, J. H. Nielsen, I. Nevo, H. Stapelfeldt, F. Filsinger, J. Küpper, and G. Meijer, Phys. Rev. Lett. **102**, 023001 (2009).
[28] B. Friedrich and D. Herschbach, Phys. Rev. Lett. **74**, 4623 (1995).
[29] B. Friedrich and D. Herschbach, J. Phys. Chem. **99**, 15686 (1995).
[30] C. Leichtle, I. Sh. Averbukh, and W. P. Schleich, Phys. Rev. Lett. **77**, 3999 (1996).
[31] T. Seideman, Phys. Rev. Lett. **83**, 4971 (1999).
[32] D. J. Tannor, *Introduction to Quantum Mechanics: A Time-Dependent Perspective*, (University Science Book, Sausalito, CA, 2007).
[33] Y. Ohtsuki and K. Nakagami, Phys. Rev. A **77**, 033414 (2008).
[34] K. Nakagami, Y. Mizumoto, and Y. Ohtsuki, J. Chem. Phys. **129**, 194103 (2008).
[35] A. P. Peirce, M. A. Dahleh, and H. Rabitz, Phys. Rev. A **37**, 4950 (1988).
[36] R. Kosloff, S. A. Rice, P. Gaspard, S. Tersigni, and D. J. Tannor, Chem. Phys. **139**, 201 (1989).
[37] K. P. Huber and G. Hertzberg, *Molecular Spectra and Molecular Structure IV: Constants of Diatomic Molecules* (Van Nostrand Reinhold, New York, 1979).
[38] G. Maroulis, J. Chem. Phys. **118**, 2673 (2003).
[39] A. Pe'er, E. A. Shapiro, M. C. Stowe, M. Shapiro, and J. Ye, Phys. Rev. Lett. **98**, 113004 (2007).
[40] E. A. Shapiro, A. Pe'er, J. Ye, and M. Shapiro, Phys. Rev. Lett. **101**, 023601 (2008).
[41] W. Shi and S. Malinovskaya, Phys. Rev. A **82**, 013407 (2010).